

Three-dimensional visualization of *planta* clathrin-coated vesicles at ultrastructural resolution

Alexander Johnson^{1,*}, Walter A. Kaufmann¹, Christoph Sommer¹, Tommaso Costanzo¹, Dana A. Dahhan², Sebastian Y. Bednarek² and Jiří Friml¹

¹Institute of Science and Technology Austria (ISTA), 3400 Klosterneuburg, Austria

²UW-Madison, Department of Biochemistry, 433 Babcock Dr., Madison, WI 53706, USA

*Correspondence: Alexander Johnson (alexander.johnson@ist.ac.at)

<https://doi.org/10.1016/j.molp.2022.09.003>

ABSTRACT

Biological systems are the sum of their dynamic three-dimensional (3D) parts. Therefore, it is critical to study biological structures in 3D and at high resolution to gain insights into their physiological functions. Electron microscopy of metal replicas of unroofed cells and isolated organelles has been a key technique to visualize intracellular structures at nanometer resolution. However, many of these methods require specialized equipment and personnel to complete them. Here, we present novel accessible methods to analyze biological structures in unroofed cells and biochemically isolated organelles in 3D and at nanometer resolution, focusing on *Arabidopsis* clathrin-coated vesicles (CCVs). While CCVs are essential trafficking organelles, their detailed structural information is lacking due to their poor preservation when observed via classical electron microscopy protocols experiments. First, we establish a method to visualize CCVs in unroofed cells using scanning transmission electron microscopy tomography, providing sufficient resolution to define the clathrin coat arrangements. Critically, the samples are prepared directly on electron microscopy grids, removing the requirement to use extremely corrosive acids, thereby enabling the use of this method in any electron microscopy lab. Secondly, we demonstrate that this standardized sample preparation allows the direct comparison of isolated CCV samples with those visualized in cells. Finally, to facilitate the high-throughput and robust screening of metal replicated samples, we provide a deep learning analysis method to screen the “pseudo 3D” morphologies of CCVs imaged with 2D modalities. Collectively, our work establishes accessible ways to examine the 3D structure of biological samples and provide novel insights into the structure of plant CCVs.

Key words: *Arabidopsis thaliana*, clathrin-coated vesicles, STEM tomography, electron microscopy, clathrin-mediated endocytosis

Johnson A., Kaufmann W.A., Sommer C., Costanzo T., Dahhan D.A., Bednarek S.Y., and Friml J. (2022). Three-dimensional visualization of *planta* clathrin-coated vesicles at ultrastructural resolution. *Mol. Plant*. **15**, 1533–1542.

INTRODUCTION

Cellular processes are reliant upon the assembly and arrangement of organelles and macromolecular complexes. By defining the three-dimensional (3D) structure of these organelles and complexes we can gain critical insights into their physiological mechanisms and functions. This high-resolution 3D imaging of biological samples with nanometer resolution is routinely achieved by combining electron microscopy (EM) with tomographic acquisition protocols (McIntosh et al., 2005). An elegant and extremely useful methodology to prepare biological samples suitable for EM tomography is the metal replication of unroofed cells, which allows the direct visualization of the intracellular landscape and subcellular organelles *in vivo*

(Heuser, 1980; Hawes and Martin, 1986; Sochacki and Taraska, 2017; Moulay et al., 2020; Johnson et al., 2021). However, to examine these samples at nanometer resolution via transmission EM, the samples must be on an EM grid. As many of the sample preparation methods used for EM tomographic analysis of unroofed cells rely upon initially plating the cells onto glass coverslips, the resulting metal replicas must be transferred to EM grids by dissolving the glass with corrosive acids (Sochacki and Taraska, 2017; Moulay et al., 2020); this procedure must be conducted by facilities with specialized

Published by the Molecular Plant Shanghai Editorial Office in association with Cell Press, an imprint of Elsevier Inc., on behalf of CSPB and CEMPS, CAS.

equipment and highly trained personnel, which restricts their wider use and application.

Clathrin-coated vesicles (CCVs) in mammalian cells are a good example of a well-characterized organelle; their structures have been defined using EM methodologies for over 50 years (Robinson, 2015). Consequently, we have a good understanding of their structural details and physiological functions in mediating cellular trafficking through the encapsulation of cargo in spherical membrane vesicles coated by a clathrin lattice (Cheng et al., 2007; Robinson, 2015; Kaksonen and Roux, 2018; Kovtun et al., 2020). This clathrin lattice, composed of repeating clathrin triskelia formed of clathrin heavy and light chains, is arranged into pentagon and hexagon panels (resembling a honeycomb pattern) to create a 3D spherical coat/cage covering the vesicle (Crowther et al., 1976; Ungewickell and Branton, 1981; Fotin et al., 2004). These CCVs are essential trafficking organelles formed during clathrin-mediated endocytosis, where they mediate cargo entry into the cell, and during post Golgi-trafficking to regulate protein sorting (Orci et al., 1985; Perez-Gomez and Moore, 2007; Hirst et al., 2012; Kaksonen and Roux, 2018). In stark contrast, while CCVs are also essential in plants (Dhonukshe et al., 2007; Perez-Gomez and Moore, 2007), we know very little about their structural and functional details. A major reason for this is because many of the standard EM sample preparation methods established in other model systems fail to reliably preserve *planta* CCVs. Furthermore, the transmission EM images of plant CCVs have been limited to planar 2D views (Dhonukshe et al., 2007; Li et al., 2012; Safavian and Goring, 2013). Therefore, due to a lack of suitable methodologies, a robust examination of the 3D structures of plant CCVs has been lacking.

To resolve the reliance on methodologies that require specialist handling of acids capable of dissolving glass and to facilitate the 3D analysis of plant CCVs at high resolution, we set out to establish methods accessible to any routine EM lab. Using *Arabidopsis thaliana* CCVs as a model organelle, we describe an accessible and standardized metal replication method that can be performed directly on EM grids, thereby removing the requirement for specialist equipment and personnel to handle extremely corrosive and hazardous reagents and enabling more researchers to visualize biological samples in 3D at high resolution. We demonstrated that this standardized method produces 3D tomographic representations of single CCVs and allows the direct comparison of CCVs in unroofed cells with biochemically isolated CCVs, finding several subtle structural differences between endocytic and biochemically isolated CCVs. In addition, we developed a semi-automated deep learning-based method that allows the robust high-throughput 3D morphological examination of CCVs and validate this approach by examining CCV structures in cells subjected to disruption of the endocytosis membrane-bending machinery.

RESULTS

Establishing scanning transmission EM tomography of CCVs in unroofed protoplasts derived from *Arabidopsis* seedlings (extended method 1)

The unreliable preservation of plant CCVs *in situ* has hampered the characterization of these structures by EM methodologies.

However, to overcome this we recently established a protoplast metal replica unroofing assay that reliably preserves large numbers of CCVs in plant cells (Narasimhan et al., 2020; Johnson et al., 2021). In this assay, cells are attached to a glass coverslip, “unroofed” (physically disrupted) to remove any cellular materials not associated with the plasma membrane (PM) directly attached to the coverslip, fixed, and coated with platinum; thus, a metal replica of the inside cellular environment of plant cells is produced, which can then be examined with EM. As this approach relied upon the use of glass coverslips, visualization of CCVs was limited to 2D views and lacked the sufficient resolution to clearly determine the arrangement of the clathrin coat lattice. While we were able to overcome these issues to produce tomographic visualizations of single CCVs (Johnson et al., 2021), we relied upon a specialist nanofabrication facility to use hydrofluoric acid to transfer the replicas from glass to EM grids—which is not feasible for many research labs. Thus, to further advance our understanding of the ultrastructural details of plant CCVs, we developed a method to produce high-resolution 3D tomographic reconstructions of CCVs in plant cells directly adhered onto EM grids. The latter is similar to previous successful methods to unroof protoplast on EM grids (Marchant and Hines, 1979; Doohan and Palevitz, 1980; van der Valk et al., 1980; Fowke et al., 1983; Traas, 1984). To do this, we developed and combined a unique range of newly optimized sample preparation steps, which critically also bypasses the requirement for corrosive acids to dissolve glass coverslips, to allow EM-capable laboratories to contribute to the collective knowledge of plant CCVs.

We focused our method on utilizing protoplast cells derived directly from *A. thaliana* seedlings (Figure 1A). As the cells are prepared and processed directly upon EM grids, a critical step of the method relies upon the cells having a good attachment to the Formvar film on the EM grid. This is because the cells need to adhere strongly enough to remain attached during multiple washing steps and still have a section of the PM attached during the physical unroofing step. We chose to utilize gold EM grids with a Formvar film to remove the possibility of metal toxicity during the incubation steps of this method. Then we treated these EM grids with a carbon and poly-L-lysine coat to aid the attachment of the cells, which was achieved by letting the cells settle into the grid during a 3-h incubation (Supplemental Figure 1). Once attached, because of their small surface area and the fragility of the EM grids subsequent sample preparation steps were conducted on small droplets of the various solutions on parafilm sheets. This also enables experimenters to process multiple samples with small volumes of reagents and materials.

Given the fragility of the EM grids, it was not possible to unroof the cells with mechanical disruption methods such as sonication, which is typically used in unroofing protocols (Sochacki and Taraska, 2017). Therefore, we relied upon the application of a detergent (Triton X-100) with gentle agitation of the samples to disrupt the cellular membranes. In addition, to dehydrate the samples rapidly without risking damage to the EM sample grids, we manually applied hexamethyldisilane rather than relying on a critical point dryer device (Shively and Miller, 2009), which sometimes damaged the grids in our experience.

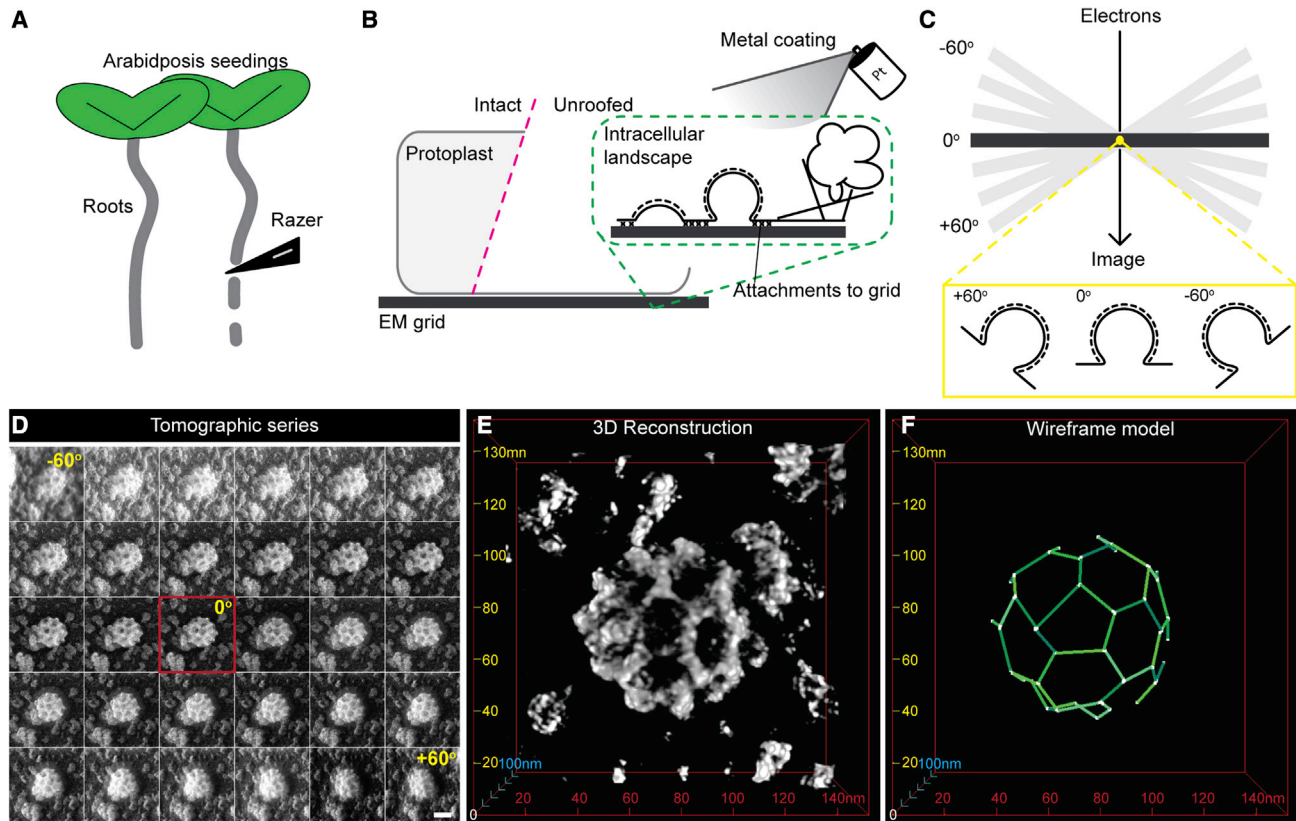


Figure 1. STEM tomography of CCVs in metal replicas of unroofed protoplasts derived from *Arabidopsis* seedlings.

- (A) Roots from *Arabidopsis thaliana* seedlings are dissected and treated to produce protoplast cells.
 (B) The cells are then attached directly to EM grids and unroofed (magenta dashed line) such that only the plasma membrane and its associated structures remain attached to the EM grid. The sample is then coated with metal to make a replica of the intracellular landscape.
 (C) The replica is visualized using EM tomography, where the sample is tilted through a series of angles allowing many perspectives of CCVs to be acquired (yellow dashed box).
 (D) Example STEM tomogram of a CCV in a metal replica of an unroofed *Arabidopsis* root protoplast. Scale bar corresponds to 50 nm.
 (E) A 3D reconstruction of (D).
 (F) A wireframe model of the reconstructed tomogram is produced to enable quantification of the structural details of the CCV.

Critically, we observed no obvious artifacts or defects in the overall cellular structure, or that of CCVs, in samples chemically dried with hexamethyldisilane compared with our previous work producing metal replicas of unroofed protoplasts which utilized critical point drying (Johnson et al., 2020, 2021; Narasimhan et al., 2020). The samples were coated with platinum to produce a replica of the unroofed cell, and an additional layer of carbon was applied to enhance the stability of the sample and to prevent electron contamination during image acquisition (Figure 1B).

To visualize the metal replicas of the unroofed cells and to capture 3D images of the CCVs, we employed scanning transmission electron microscopy (STEM) tomography. We focused exclusively on CCVs formed during clathrin-mediated endocytosis by examining only PM-associated CCVs. Tomograms of individual CCVs were generated by tilting the EM grid through a range of angles (typically -72° to $+72^\circ$) along a single tilt axis, and images from each perspective were acquired (Figure 1C and 1D). The tomogram images were aligned by cross-correlation and used to create a 3D visualization of the CCV (Figure 1E and Supplemental Video 1). From these 3D reconstructions we were able to

precisely determine the structural details of the CCVs, such as diameters, volumes, arrangement of clathrin lattices, and lengths of the triskelia arms, by making wireframe models of the CCVs (Figure 1F and Supplemental Table 1). As such, we found that the average *A. thaliana* root cell endocytic CCV has a diameter of 75.99 ± 0.63 nm, volume of $1868.5 \pm 45.54 \mu\text{m}^3$, and 17 clathrin panels (5 pentagons, 4 hexagons, and 8 not fully visibly closed at the base of the CCV) with a branch arm length of 16.88 ± 0.06 nm.

Thus, we established an accessible user-friendly “on-grid” metal replication method, which removes the requirement to chemically dissolve glass coverslips, allowing the direct 3D STEM imaging of CCVs in cells at nanometer resolution, thereby revealing details of the *planta* CCV clathrin coat arrangements.

3D analysis of biochemically isolated CCVs prepared using the on-grid protocol (extended method 2)

To demonstrate the versatility of the on-grid metal replication protocol, we examined the 3D ultrastructure of CCVs biochemically isolated from plant cells. Here, we employed the same method for preparing unroofed cells to prepare and visualize

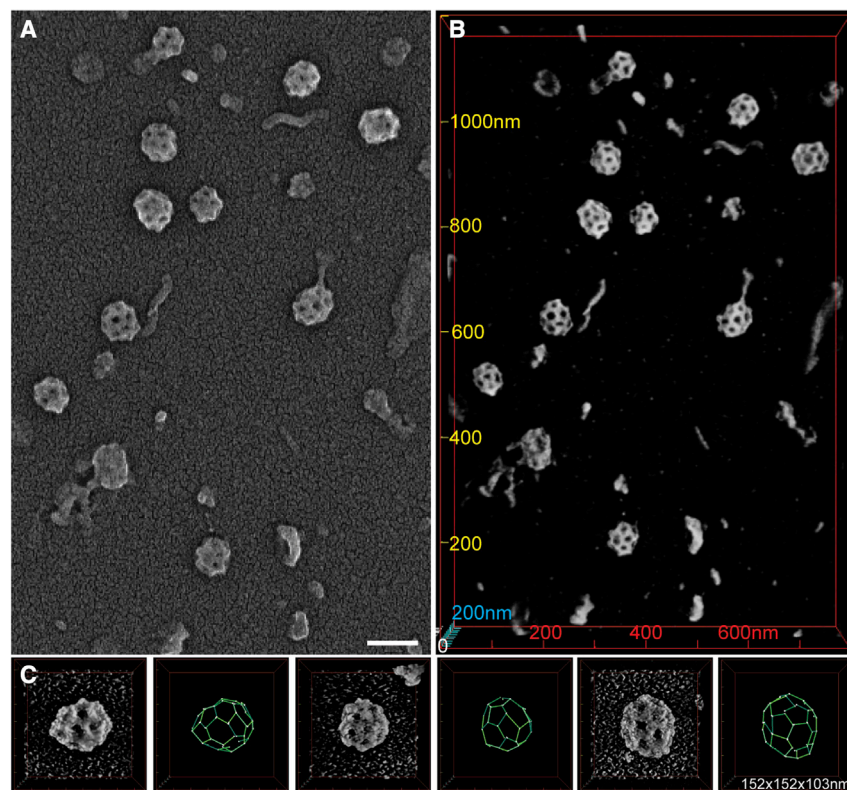


Figure 2. Application of the standardized “on-grid” metal replication method to visualize biochemically isolated CCVs in 3D.

(A) Example STEM image of metal replicas of isolated CCV preparations from *Arabidopsis* T87 suspension cell cultures. Scale bar corresponds to 100 nm.

(B) A 3D reconstruction of **(A)**. Scale values are reported as nm.

(C) Representative 3D reconstructions and wire-frame models of single CCVs. 3D volume; x = 152, y = 152, and z = 103 nm.

examine large numbers of CCV structures, we developed a deep learning-based method to analyze the morphology of CCVs from images acquired at lower resolutions and in a single plane using a scanning electron microscope. This morphologic analysis enables rapid and robust “pseudo 3D” analyses of CCVs and their formation in a high-throughput and unbiased manner.

To develop this method, we used images of metal replicas of unroofed protoplasts derived from *A. thaliana* root cells attached to glass coverslips (Johnson et al., 2021). Here, as the metal replicas were imaged in 2D with a large field of view using scanning electron

microscopy (SEM), each image contained many visible CCVs enabling the high-throughput visualization of CCVs. To characterize the morphology of the CCVs, we quantified various object features such as area, maximum and minimum diameters, and average gray value. To date, such analysis has relied upon manual segmentation of the CCVs by the experimenter. To increase the throughput and reproducibility of the morphology quantification of CCVs, we used deep learning to create an accurate CCV segmentation model. To do this, we created a comprehensive training set of image pairs consisting of raw images together with the same images in which the CCVs were manually annotated (Figure 3A). This training dataset was then used to train a state-of-the-art neural network model called Cellpose to generate an accurate CCV prediction model (Stringer et al., 2021). To increase the robustness and the ability of the model to predict all possible CCV structures, the training set included images of metal replicas of unroofed cells derived from wild-type plants and from a mutant that produces clathrin plaques (which are absent from wild-type cells [Johnson et al., 2020; Narasimhan et al., 2020; Johnson et al., 2021]). The trained model was then used to automatically detect CCVs in additional images that had not previously been seen by the model (“unseen images”) (Figure 3B). To validate the model predictions, we compared the automated segmentations with manual segmentations for a dataset of CCVs from wild-type cells. From 17 SEM images of metal replicas of unroofed cells, manual segmentation identified 234 CCVs, whereas the automated method successfully predicted 232 (Supplemental Table 3). To determine if the CCV segmentations from our model matched those made manually, we calculated the average pixel overlap between the manual and automated CCV segmentations using an intersection

purified CCV preparations, allowing the direct comparison of isolated and *in vivo* organelles, such as purified CCVs and *bona fide* endocytic CCVs.

CCVs were isolated from undifferentiated *Arabidopsis* suspension cell cultures (Reynolds et al., 2014) and attached directly to glow discharged and carbon-coated EM mesh grids. The samples were then processed with the same methodology as unroofed cells. Imaging the metal replicas of purified CCVs with STEM tomography allowed the production of 3D reconstructions of the isolated CCVs (Figure 2A and 2B, Supplemental Video 2), enabling their quantitative structural analysis (Figure 2C). We found that the average isolated CCV was 71.06 ± 1.65 nm in diameter, 1547.45 ± 110.64 μm^3 in volume, and consisted of 17 clathrin panels (6 pentagons, 4 hexagons, and 7 not fully visibly closed at the base of the CCV) with a branching arm length of 18.22 ± 0.14 nm (Supplemental Table 2).

This demonstrates the versatility of the on-grid metal replication methodology and provides a standardized method to structurally characterize CCVs from different biological sources in 3D using STEM tomography.

High-throughput pseudo 3D morphology screening of CCVs (extended method 3)

While tomographic reconstruction of single CCVs enables the direct visualization of their 3D structure and morphology at high resolution, it is a low-throughput approach and requires access to high-end STEM microscopes. Thus, to increase our ability to

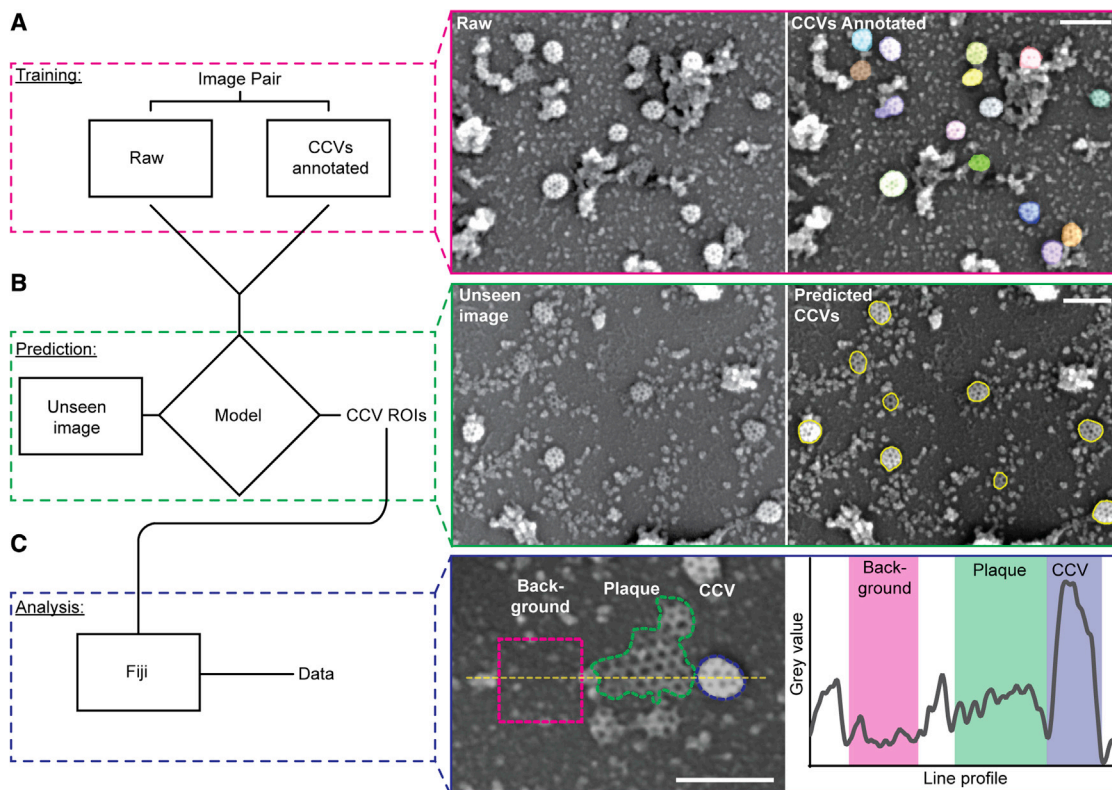


Figure 3. High-throughput deep learning analysis of CCV pseudo-3D morphology.

(A) Model training: example image from the training set with manual annotation (left-hand image, multiple colors) overlaid with metal replicas of unroofed *Arabidopsis* root protoplasts acquired by SEM.

(B) Model prediction: the model is used to predict CCVs in images not included in the training set (“unseen image”). These predictions are outputted as a series of ROIs of CCVs (yellow outlines).

(C) The predicted CCV ROIs are opened in Fiji to quantify morphological features of each CCV. Blue box: a pseudo 3D metric is provided by the gray value of the CCV, as the more spherical a CCV is, the higher its gray value; the gray values of the PM (magenta dashed line), a clathrin plaque (green dashed line), and typical CCV (blue dashed line) are measured along the yellow dashed line and quantified on the left plot. Scale bars correspond to 200 nm.

over union (IoU) calculation (Supplemental Figure 2). The overlap was 83%, indicating that the Cellpose model predicted the same CCV structures and with high degree of accuracy. The predicted CCV segmentations were then exported as regions of interest (ROIs) to Fiji and quantified. This Fiji analysis step was not automated to provide a checkpoint for users to visualize and confirm the automated CCV segmentations. We found that the average areas reported by manual and automated analyses were not significantly different (t test, $p = 0.35$) ($4.93 \pm 0.21 \mu\text{m}^2$ [diameter of 79.24 nm] for the manual segmentations and $5.24 \pm 0.25 \mu\text{m}^2$ [diameter of 81.71 nm] for the automated segmentations [Supplemental Table 3]), thus validating the accuracy of this approach.

To provide a pseudo 3D metric, CCV curvature, the average gray value of the CCV was used as a proxy for how spherical/3D the CCV was. During its development, the CCV becomes more protein dense and projects away from the PM, yielding a higher gray value than flat structures on the PM (Moulay et al., 2020) (Figure 3C). By normalizing the CCV gray values to an area of flat PM in each image, we could generate relative estimates of 3D curvature and compare them across different images. Comparing the curvature estimation from the manual and automated segmentations from the validation wild-type data re-

sulted in similar values: 2.23 ± 0.07 arbitrary units (a.u.) for manual and 2.19 ± 0.07 a.u. for automated segmentations (Supplemental Table 3).

To highlight the robustness of this method in identifying and screening the pseudo 3D morphology of CCVs in a high-throughput manner, we applied it to SEM images of unroofed cells in which the clathrin-mediated endocytosis membrane-bending machinery was disrupted (Figure 4A). These images were of metal replicas of unroofed protoplasts derived from the roots of *WDXM2* seedlings, an inducible loss-of-function TPLATE mutant that prevents the formation of spherical CCVs (Johnson et al., 2021; Wang et al., 2021), subjected to control (non-induction) and disruptive (induced) conditions. The automated segmentation successfully detected the clathrin structures under both experimental conditions, finding one additional CCV compared with manual segmentation for each condition. The IoU pixel overlap was 92% when comparing the manual and automated segmentations (Supplemental Table 4), indicating that the structures identified had a high degree of overlap. The area and the estimated 3D curvature values of each CCV were plotted against each other for each experimental condition (Figure 4B), revealing the 3D morphological differences of the CCVs in control and

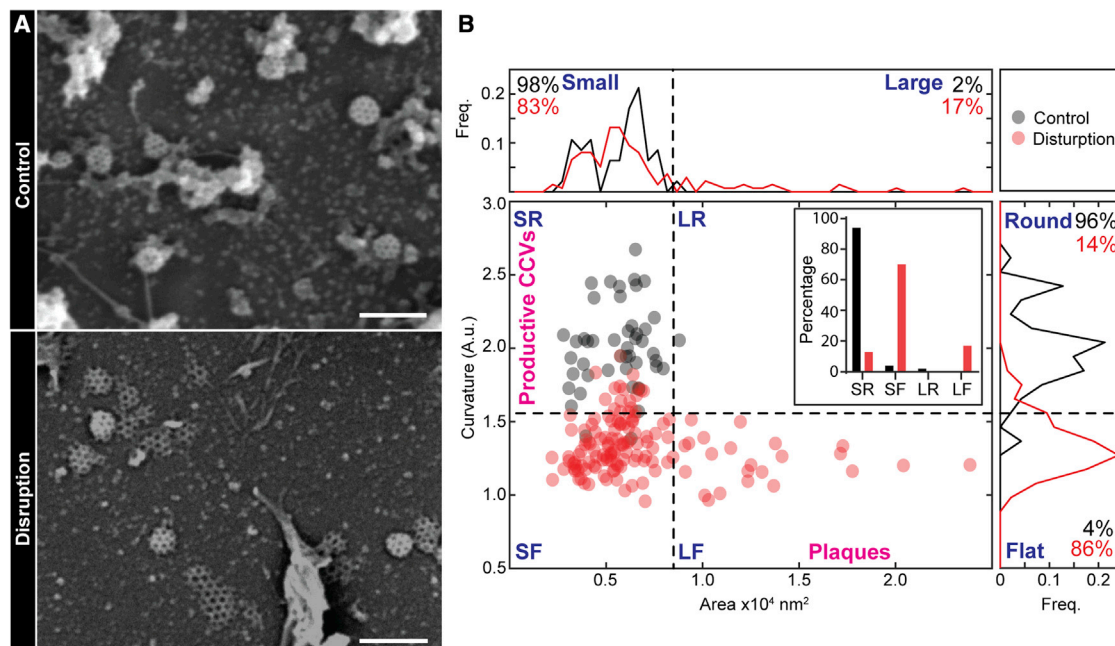


Figure 4. Deep learning analysis of CCV morphology during endocytic membrane-bending disruption.

(A) Example SEM images of metal replicas of unroofed protoplasts derived from roots of *WDXM2* seedlings subjected to control or membrane-bending disruptive conditions. Scale bars correspond to 200 nm.

(B) Quantification of CCV morphology as detected using our deep learning-based analysis in control (black) or disruptive (red) conditions. Histograms (upper and right panels) and scatter plot (bottom left panel) of the areas and estimated 3D curvature of CCVs in control (black) or disruptive (red) conditions. Thresholds are used to classify the CCVs (black dashed lines) into categories based on their 3D shape; SR, small and round, representing productive endocytic CCVs; SF, small and flat; LR, large and round; and LF, large and flat, representing plaques. The percentage of CCVs in each category is shown in the insert bar graph. N: control, 47 CCVs; disruption, 131 CCVs.

membrane-bending disruptive conditions. To further define these morphological differences, we imposed thresholds upon the data (Moulay et al., 2020). First, an area threshold of 8500 nm^2 (diameter of $\sim 105 \text{ nm}$) was used to classify clathrin structures as “large” or “small.” To classify clathrin structures based on their 3D shape, we identified “curved” or “flat” structures, which were defined by the average curvature estimation of the three flattest CCVs visible in the control conditions determined manually (1.54 a.u.). Combining these thresholds created four morphological categories to define the clathrin structures: small and round (SR) representing productive endocytic CCVs, small and flat (SF), large and round (LR), and large and flat (LF) representing plaques. We found that the majority of CCVs formed during the control conditions were classed within the SR category (94% compared with 13% during disruption), whereas the majority of CCVs formed during membrane-bending disruption were classified as SF (70% compared with 4% in the control) (Figure 4B). This agrees with our previous results examining CCVs in metal replicas of unroofed *WDMX2* protoplasts (Johnson et al., 2021), which were based upon time-consuming manual segmentation and high-resolution STEM tomography, therefore confirming the utility of the automated segmentations for high-throughput screening of the pseudo 3D morphology of CCVs.

DISCUSSION

Understanding the structural details of biological samples provides key insights into their functions; therefore, high-resolution

3D imaging is an extremely powerful tool for investigating cell biology. While EM techniques are routinely used to achieve this, they are traditionally often reliant upon harsh and/or dangerous chemicals requiring specialized facilities to conduct them (Sochacki and Taraska, 2017; Johnson et al., 2021), which can limit their accessibility to the biological community. To overcome this, we developed methods that allow the 3D examination of metal replicated samples in any routine EM lab (Figure 5). Specifically, we provide a method for preparing samples (unroofed cells and biochemically isolated organelles) directly on EM grids, providing a standardized sample preparation methodology that does not require the use of extremely toxic acids. These preparations can be combined with STEM tomography to produce nanometer-resolution 3D images. However, as this high-resolution imaging can be time consuming, we also developed a high-throughput deep learning-based analysis method that enables rapid morphological pseudo 3D screening of biological structures. While these methods can likely be adjusted for a range of cell types and organelles, here we applied them to further characterize the 3D morphology of plant CCVs which are an essential trafficking organelles underpinning many cellular processes (Chen et al., 2011)—at high resolution. We first visualized the clathrin assembly of CCVs in unroofed protoplasts to investigate endocytic CCV structures. Interestingly, while CME is a multiple-step process during which the CCV dramatically changes shape (initiation [flat], invagination [dome shape], to spherical [omega shape]) (Kaksonen and Roux, 2018), we saw little variety within the endocytic CCV structures present in our

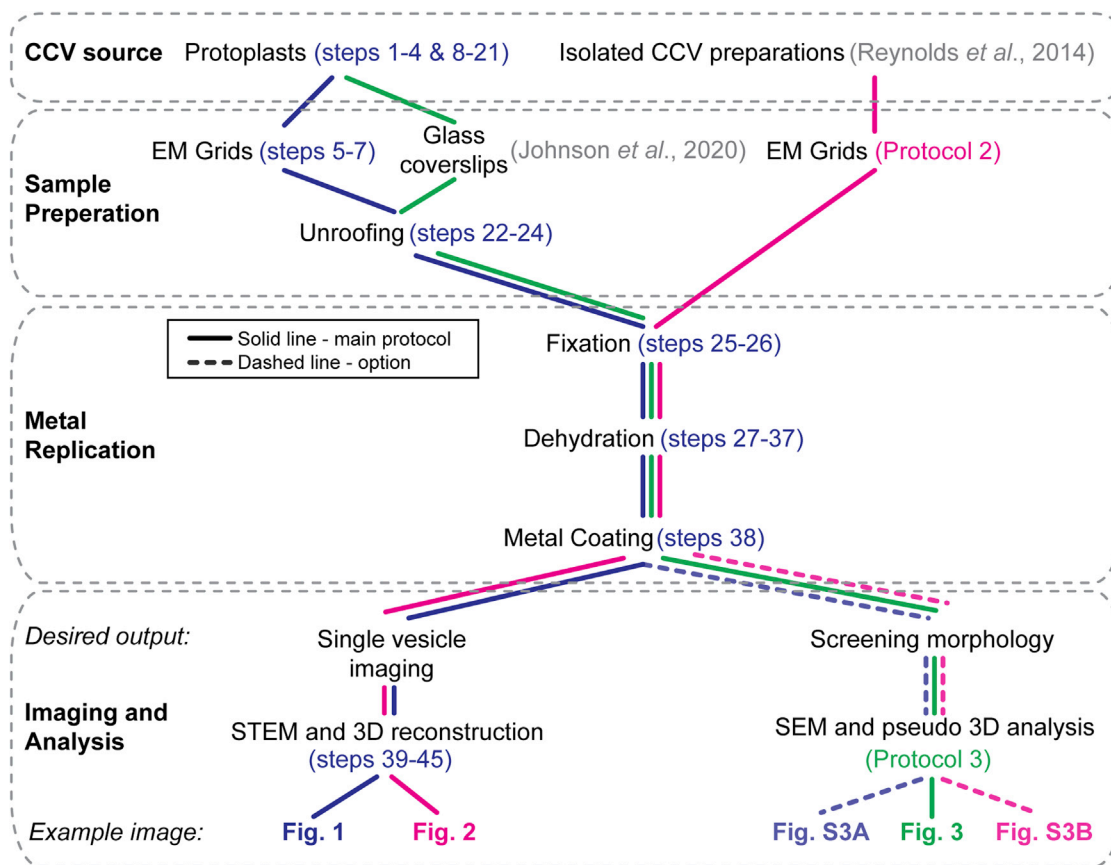


Figure 5. Overview of the methods developed to examine plant CCVs in 3D.

Flow chart showing the versatility of the presented protocols to visualize CCVs in 3D. Steps refer to the detailed step-by-step protocols included in the [supplemental materials and methods](#) (blue: extended method 1—STEM tomography of unroofed protoplast cells derived from *Arabidopsis* seedlings; magenta: extended method 2—STEM tomography of isolated CCVs derived from cultured *Arabidopsis* cells; green: extended method 3—high-throughput pseudo 3D morphological screening of CCVs).

protoplast cells. This is likely due to the stability and energetic cost of formation of the various structures. Recently, biophysical models determined that the omega-shaped endocytosis stage of CCV formation was the most energetically stable stage (Ma and Berro, 2021); thus, this would explain why we readily detected CCVs representing this state. By using the same sample preparation method for biochemically isolated CCVs, we could directly compare them to specific CCV populations visualized inside cells. While we found that there were small differences in the sizes of endocytic and isolated CCVs, this is likely due to the fact that the isolated CCV preparations from whole-cell lysates contain a mixture of CCVs derived from different origins - clathrin-mediated endocytosis and the early endosome/trans-Golgi network (Reynolds *et al.*, 2014; Mosesso *et al.*, 2018; Dahhan *et al.*, 2022). Finally, we provide a robust workflow that allows the high-throughput pseudo 3D morphological screening of organelles in unroofed cells, enabling robust quantitative analysis of CCVs in cells subjected to physiological disruptions. We then validated this pseudo 3D analysis by applying it to metal replicas of unroofed cells with a inducible loss of endocytic membrane bending.

To produce samples that reliably contain *planta* CCVs, we made use of protoplasts. This is because, for an unknown reason, CCVs

are rarely preserved no matter which EM sample preparation method is used for whole-plant samples. Therefore, to enable robust quantitative analysis we had to utilize a cell system that allowed the consistent preservation of CCVs. As a result, we examined plant CCVs that formed in a different biophysical cellular environment compared with those in intact plants. However, protoplasts contain the same protein machinery responsible for producing CCVs, and the diameters of the protoplast CCVs (76 nm) are similar to the few reported measurements made in intact plant tissues (~80 nm) (Dhonukshe *et al.*, 2007; Li *et al.*, 2012), thus highlighting that the difference in cellular environments does not affect the overall production of CCVs.

We focused on utilizing protoplasts derived directly from *Arabidopsis* seedlings. This allows one to use already existing and established genetically altered plants as starting material. Furthermore, it provides the opportunity to reliably examine the effect of mutants upon CCV formation and structure. For example, STEM tomography was recently used to examine CCVs in a plant with inducible loss of function of an essential endocytic protein (Johnson *et al.*, 2021; Wang *et al.*, 2021). The use of homozygous *Arabidopsis* seedlings ensures that every unroofed cell carries the genetic manipulation, which is not possible to guarantee using transient transfection protocols,

which are not 100% efficient; furthermore, while our method reliably produces unroofed cells with visible CCVs, it is also not 100% efficient (e.g., we typically experienced an unroofing success rate of ~58%, and 12.4% of these cells contained multiple examples of CCVs).

Our high-throughput screen of CCV pseudo 3D morphology was performed using samples attached to glass coverslips. This demonstrates that 3D analysis of samples can be conducted even without high-end STEM-enabled microscopes. To test the versatility of this analysis we applied the same CCV segmentation model to SEM images of metal replicas of unroofed protoplasts prepared directly on EM grids (extended method 1) and to isolated CCVs (extended method 2) (Supplemental Figure 3). We found that the model was accurate for both the in-cell and purified CCVs. However, to further improve this accuracy, we suggest training specialized models using representative CCV images of the specific preparation method of interest.

We also expect our methods to become a platform for further technical innovations and optimizations to continue advancing our understanding of these critical trafficking organelles. For example, combining these methods with immunolabeling approaches and fluorescence super-resolution microscopy, such as correlated light and electron microscopy procedures, would help to unravel the molecular composition of CCVs and allow the precise localization of CCV-related proteins. These sample preparation methods could also aid researchers to further develop focused ion beam milling and cryo-EM approaches to capture images of CCVs *in situ* inside a range of plant tissues, such as efforts to conduct focused ion beam milling on *Arabidopsis* pollen tubes (Liu et al., 2021).

Overall, we present refined accessible user-friendly methods for the 3D analysis of biological samples and investigate the 3D structural details of plant CCVs at unprecedented resolution and accuracy. The experimental methods provide the opportunity for the direct comparison of CCVs derived from different sources, such as specific cell types and purified CCV preparations. In addition, the methods allow one to define individual structures at high resolution and screen CCVs using high-throughput machine learning-assisted analysis to robustly quantify their morphology.

METHODS

For detailed step-by-step protocols of the methodologies presented in this article (extended method 1, STEM tomography of unroofed protoplast cells derived from *Arabidopsis* seedlings; extended method 2, STEM tomography of isolated CCVs derived from cultured *Arabidopsis* cells; and extended method 3, high-throughput pseudo 3D morphological screening of CCVs), please refer to the [supplemental experiential procedures](#).

Plant materials and sample preparation

To generate *Arabidopsis* root protoplasts, *Arabidopsis thaliana* Col-0 seeds were sown on 1/2 AM agar plates, supplemented with 1% (w/v) sucrose. The plates were stratified by incubation at 4°C for 2–3 days in the dark and then grown vertically for 8–10 days (21°C; 16 h light and 8 h dark cycle). The roots were dissected from the seedlings and then cut into small sections (~1–2 mm) in enzyme solution (0.4 M mannitol, 20 mM KCl, 20 mM MES [pH 5.7], 1.5% cellulase R10 [Duchefa no.

C8001], and 0.4% macerozyme R10 [Serva no. 28302] in H₂O). The enzyme solution and sections were then incubated in a vacuum chamber for 20 min and then incubated at room temperature and atmospheric pressure in the dark with gentle agitation for 3 h. The cells were collected by centrifugation at 100 rcf (relative centrifugal force) for 2 min at room temperature. The pelleted cells were washed with W5 buffer (154 mM NaCl, 125 mM CaCl₂, 5 mM KCl, and 2 mM MES) by centrifugation (100 rcf for 2 min). The cells were resuspended in W5 buffer and incubated at 4°C for 30 min. The cells were then centrifuged (100 rcf for 2 min) and resuspended in hyperosmotic growth media buffer (0.44% [w/v] MS powder with vitamins [Duchefa no. M0222], 89 mM sucrose, and 75 mM mannitol [pH 5.5], adjusted with KOH) and plated on pre-prepared EM grids (detailed in the following section), on which they were incubated in a humid chamber for 3 h. The cells were then washed with PBS. To unroof the cells, the samples were incubated with extraction buffer (2 μM phalloidin, 2 μM taxol, 1% [w/v] Triton X-100, and 1% [w/v] polyethylene glycol [PEG; MW 2000] in PEM buffer [100 mM PIPES free acid, 1 mM MgCl₂, 1 mM EGTA [pH 6.9 adjusted with KOH]]) for 5 min with gentle agitation. The samples were then washed three times with PEM buffer supplemented with 1% (w/v) PEG 2000. Samples were fixed using 2% (w/v) glutaraldehyde (GA) in 0.1 M phosphate buffer (PB) via a 30-min incubation. The samples were then washed twice with 0.1 M PB and stored in 0.1 M PB at 4°C until further processing.

Purified CCV samples were isolated from undifferentiated T87 *Arabidopsis* suspension cell cultures by differential gradient centrifugation, as described previously (Reynolds et al., 2014). Five microliters of the CCV preparation (0.33 mg/ml) was plated and incubated on a pre-prepared EM grid (detailed in the following section) for 4 min. Whatman blotting paper was used to remove the excess solution. The samples were then fixed with 2% GA in 0.1 M PB via a 30-min incubation.

EM grid preparations

Gold EM grids with Formvar film (Electron Microscopy Sciences no. G300PB-Au) were used for processing protoplast samples. The grids were coated with carbon to a thickness of 10 nm using a Leica ACE600 coating device. The grids were then supplemented with poly-L-lysine (Sigma) in a 15-min incubation and washed with H₂O.

Copper EM grids with carbon-film (Electron Microscopy Sciences no. CF300-Cu) were used for isolated CCV preparations. The grids were subjected to glow discharge (4 min at 7 × 10⁻¹ mbar) using the ELMO glow discharge system (Agar Scientific).

Metal replication of samples

The fixed samples were washed with 0.1 M PB and H₂O, and then incubated with 0.1% (w/v) tannic acid for 20 min. The samples were washed three times with H₂O and incubated with 0.2% (w/v) uranyl acetate for 20 min. To dehydrate the samples, they were washed three times with H₂O, infiltrated with graded ethanol (10%, 20%, 40%, 60%, 80%, 96%, and 100%), and subjected to a 2-min incubation with hexamethyldisilane. The samples were then dried by evaporation and subsequently coated with 3 nm platinum and 4 nm carbon using the ACE600 coating device (Leica Microsystems).

STEM tomography

STEM tomograms were acquired with a JEOL JEM2800 STEM (200 kV AV) controlled by a STEM Recorder (<https://temography.com/en/>). Diameters of the CCVs were determined from the 0° single-plane STEM image, and an average value was calculated from the maximum and minimum Feret distances of a ROI drawn around the CCV in Fiji (Schindelin et al., 2012). This value was then used to calculate a spherical volume. Tomograms of single CCVs were recorded over a range of ~ -72° to +72° along single tilt axis with a step size of 4°. The tomograms were aligned and reconstructed using Composer (<https://temography.com/en/>). Wireframe models of the CCVs were manually created using Evo-viewer

(<https://tomography.com/en/>) and used to quantify aspects of the CCV structure. Data were collected from at least two repeats. Reported quantitative measurement values in the main text are reported as mean \pm SEM.

High-throughput pseudo 3D morphology screening of CCVs

SEM images of metal replicas of unroofed protoplasts (derived from *A. thaliana* seedling roots) taken with an FE-SEM Merlin Compact VP equipped with an In-lens Duo detector, were obtained from Johnson et al. (2021). These images included CCVs from Col-0 and *WDMX2* protoplasts incubated in control (4-h incubation at room temperature) or endocytic membrane-bending disruptive (4-h incubation at 37°C) conditions, which were collected using the same magnification (\sim 45 k) and pixel size settings (\sim 2.4–2.6 nm). The protoplasts were prepared on glass coverslips as described previously (Johnson et al., 2021).

For the automated segmentation of CCVs, we first generated a training set consisting of 13 example image pairs (raw image and segmentation masks) of the CCVs in replica images of wild-type and *WDMX2* cells subjected to control or disruptive conditions. CCVs in the raw images were manually annotated using the Napari software (Sofroniew et al., 2022). We then trained Cellpose (Stringer et al., 2021) using input for 5000 epochs (see extended method 1 for further details). The resulting trained model was then used to segment individual CCVs. To determine the localization accuracy of the automated CCV segmentation, we calculated the mean pixel-wise IoU of manually annotated and predicted CCVs. Pixel-wise IoU is defined as the number of pixels in both the *manual* and the *predicted* CCV segmentation mask, over the number of pixels of the union of both segments.

$$IoU = \frac{|manual \cap predicted|}{|manual \cup predicted|}$$

The predicted segmentation ROIs were then exported to Fiji (Schindelin et al., 2012) to quantify the area and average gray value of each CCV. Diameters of the equivalent circle were calculated from the CCV area. To estimate the curvature/pseudo 3D of the CCV, the average gray value of the CCV ROI was normalized by dividing it by the average gray value of four manually selected PM ROIs in each image, which provided a background value of the image. The area and pseudo 3D values were plotted to define the overall morphology of a CCV. The morphologies were then divided into four categories (SR, SF, LR, and LF) using an area threshold of 8500 nm² (a CCV diameter of 105 nm) and a 3D value of 1.52 (the average of the three smallest CCVs in control conditions determined to be spherical by the experimenter).

Data availability

Example data and the code generated in this study are available at: <https://doi.org/10.5281/zenodo.6563819>.

SUPPLEMENTAL INFORMATION

Supplemental information is available at *Molecular Plant Online*.

FUNDING

A.J. is supported by funding from the Austrian Science Fund I3630B25 (to J.F.).

AUTHOR CONTRIBUTIONS

Conceptualization, A.J., W.A.K., and J.F.; methodology, A.J. and W.A.K.; investigation, A.J., W.A.K., and T.C.; software, C.S.; validation and formal analysis, A.J.; resources, D.A.D. and S.Y.B.; writing – original draft, A.J.; all authors reviewed and edited the final manuscript.

ACKNOWLEDGMENTS

This research was supported by the Scientific Service Units of Institute of Science and Technology Austria (ISTA) through resources provided by the Electron Microscopy Facility, Lab Support Facility, and the Imaging and

Optics Facility. We acknowledge Prof. David Robinson (Heidelberg) and Prof. Jan Traas (Lyon) for making us aware of previously published classical on-grid preparation methods. No conflict of interest declared.

Received: June 10, 2022

Revised: August 18, 2022

Accepted: September 6, 2022

Published: September 7, 2022

REFERENCES

- Chen, X., Irani, N.G., and Friml, J. (2011). Clathrin-mediated endocytosis: the gateway into plant cells. *Curr. Opin. Plant Biol.* **14**:674–682. <https://doi.org/10.1016/j.pbi.2011.08.006>.
- Cheng, Y., Boll, W., Kirchhausen, T., Harrison, S.C., and Walz, T. (2007). Cryo-electron tomography of clathrin-coated vesicles: structural implications for coat assembly. *J. Mol. Biol.* **365**:892–899. <https://doi.org/10.1016/j.jmb.2006.10.036>.
- Crowther, R.A., Finch, J.T., and Pearse, B.M. (1976). On the structure of coated vesicles. *J. Mol. Biol.* **103**:785–798. [https://doi.org/10.1016/0022-2836\(76\)90209-6](https://doi.org/10.1016/0022-2836(76)90209-6).
- Dahhan, D.A., Reynolds, G.D., Cárdenas, J.J., Eeckhout, D., Johnson, A., Yperman, K., Kaufmann, W.A., Vang, N., Yan, X., Hwang, I., et al. (2022). Proteomic characterization of isolated Arabidopsis clathrin-coated vesicles reveals evolutionarily conserved and plant-specific components. *Plant Cell* **34**:2150–2173. <https://doi.org/10.1093/plcell/koac071>.
- Dhonukshe, P., Aniento, F., Hwang, I., Robinson, D.G., Mravec, J., Stierhof, Y.D., and Friml, J. (2007). Clathrin-mediated constitutive endocytosis of PIN auxin efflux carriers in Arabidopsis. *Curr. Biol.* **17**:520–527. <https://doi.org/10.1016/j.cub.2007.01.052>.
- Doohan, M.E., and Palevitz, B.A. (1980). Microtubules and coated vesicles in guard-cell protoplasts of *Allium cepa* L. *Planta* **149**:389–401. <https://doi.org/10.1007/BF00571175>.
- Fotin, A., Cheng, Y., Sliz, P., Grigorieff, N., Harrison, S.C., Kirchhausen, T., and Walz, T. (2004). Molecular model for a complete clathrin lattice from electron cryomicroscopy. *Nature* **432**:573–579. <https://doi.org/10.1038/nature03079>.
- Fowke, L.C., Rennie, P.J., and Constabel, F. (1983). Organelles associated with the plasma membrane of tobacco leaf protoplasts. *Plant Cell Rep.* **2**:292–295. <https://doi.org/10.1007/BF00270184>.
- Hawes, C., and Martin, B. (1986). Deep etching of plant cells: cytoskeleton and coated pits. *Cell Biol. Int. Rep.* **10**:985–992.
- Heuser, J. (1980). Three-dimensional visualization of coated vesicle formation in fibroblasts. *J. Cell Biol.* **84**:560–583. <https://doi.org/10.1083/jcb.84.3.560>.
- Hirst, J., Borner, G.H.H., Antrobus, R., Peden, A.A., Hodson, N.A., Sahlender, D.A., and Robinson, M.S. (2012). Distinct and overlapping roles for AP-1 and GGAs revealed by the "knocksideways" system. *Curr. Biol.* **22**:1711–1716. <https://doi.org/10.1016/j.cub.2012.07.012>.
- Johnson, A., Gnyliukh, N., Kaufmann, W.A., Narasimhan, M., Vert, G., Bednarek, S.Y., and Friml, J. (2020). Experimental toolbox for quantitative evaluation of clathrin-mediated endocytosis in the plant model Arabidopsis. *J. Cell Sci.* **133**, jcs.248062. <https://doi.org/10.1242/jcs.248062>.
- Johnson, A., Dahhan, D.A., Gnyliukh, N., Kaufmann, W.A., Zheden, V., Costanzo, T., Mahou, P., Hrtyan, M., Wang, J., Aguilera-Servín, J., et al. (2021). The TPLATE complex mediates membrane bending during plant clathrin-mediated endocytosis. *Proc. Natl. Acad. Sci. USA* **118**, 2113046118. <https://doi.org/10.1073/pnas.2113046118>.
- Kaksonen, M., and Roux, A. (2018). Mechanisms of clathrin-mediated endocytosis. *Nat. Rev. Mol. Cell Biol.* **19**:313–326. <https://doi.org/10.1038/nrm.2017.132>.

- Kovtun, O., Dickson, V.K., Kelly, B.T., Owen, D.J., and Briggs, J.A.G.** (2020). Architecture of the AP2/clathrin coat on the membranes of clathrin-coated vesicles. *Sci. Adv.* **6**, eaba8381. <https://doi.org/10.1126/sciadv.aba8381>.
- Li, R., Liu, P., Wan, Y., Chen, T., Wang, Q., Mettbach, U., Baluska, F., Samaj, J., Fang, X., Lucas, W.J., et al.** (2012). A membrane microdomain-associated protein, Arabidopsis Flot1, is involved in a clathrin-independent endocytic pathway and is required for seedling development. *Plant Cell* **24**:2105–2122. <https://doi.org/10.1105/tpc.112.095695>.
- Liu, Z., Gao, J., Cui, Y., Klumpe, S., Xiang, Y., Erdmann, P.S., and Jiang, L.** (2021). Membrane imaging in the plant endomembrane system. *Plant Physiol.* **185**:562–576. <https://doi.org/10.1093/plphys/kiaa040>.
- Ma, R., and Berro, J.** (2021). Endocytosis against high turgor pressure is made easier by partial coating and freely rotating base. *Biophys. J.* **120**:1625–1640. <https://doi.org/10.1016/j.bpj.2021.02.033>.
- Marchant, H.J., and Hines, E.R.** (1979). The role of microtubules and cell-wall deposition in elongation of regenerating protoplasts of *Mougeotia*. *Planta* **146**:41–48. <https://doi.org/10.1007/BF00381253>.
- McIntosh, R., Nicastro, D., and Mastrorarde, D.** (2005). New views of cells in 3D: an introduction to electron tomography. *Trends Cell Biol.* **15**:43–51. <https://doi.org/10.1016/j.tcb.2004.11.009>.
- Mosso, N., Bläske, T., Nagel, M.K., Laumann, M., and Isono, E.** (2018). Preparation of clathrin-coated vesicles from Arabidopsis thaliana seedlings. *Front. Plant Sci.* **9**, 1972. <https://doi.org/10.3389/fpls.2018.01972>.
- Moulay, G., Laine, J., Lemaitre, M., Nakamori, M., Nishino, I., Caillol, G., Mamchaoui, K., Julien, L., Dingli, F., Loew, D., et al.** (2020). Alternative splicing of clathrin heavy chain contributes to the switch from coated pits to plaques. *J. Cell Biol.* **219**, e20191206110. <https://doi.org/10.1083/jcb.201912061>.
- Narasimhan, M., Johnson, A., Prizak, R., Kaufmann, W.A., Tan, S., Casillas-Pérez, B., and Friml, J.** (2020). Evolutionarily unique mechanistic framework of clathrin-mediated endocytosis in plants. *Elife* **9**, e52067.
- Orci, L., Ravazzola, M., Amherdt, M., Louvard, D., and Perrelet, A.** (1985). Clathrin-immunoreactive sites in the Golgi apparatus are concentrated at the trans pole in polypeptide hormone-secreting cells. *Proc. Natl. Acad. Sci. USA* **82**:5385–5389. <https://doi.org/10.1073/pnas.82.16.5385>.
- Pérez-Gómez, J., and Moore, I.** (2007). Plant endocytosis: it is clathrin after all. *Curr. Biol.* **17**:R217–R219. <https://doi.org/10.1016/j.cub.2007.01.045>.
- Reynolds, G.D., August, B., and Bednarek, S.Y.** (2014). Preparation of enriched plant clathrin-coated vesicles by differential and density gradient centrifugation. *Methods Mol. Biol.* **1209**:163–177. https://doi.org/10.1007/978-1-4939-1420-3_13.
- Robinson, M.S.** (2015). Forty years of clathrin-coated vesicles. *Traffic* **16**:1210–1238. <https://doi.org/10.1111/tra.12335>.
- Safavian, D., and Goring, D.R.** (2013). Secretory activity is rapidly induced in stigmatic papillae by compatible pollen, but inhibited for self-incompatible pollen in the Brassicaceae. *PLoS One* **8**, e84286. <https://doi.org/10.1371/journal.pone.0084286>.
- Schindelin, J., Arganda-Carreras, I., Frise, E., Kaynig, V., Longair, M., Pietzsch, T., Preibisch, S., Rueden, C., Saalfeld, S., Schmid, B., et al.** (2012). Fiji: an open-source platform for biological-image analysis. *Nat. Methods* **9**:676–682. <https://doi.org/10.1038/nmeth.2019>.
- Shively, S., and Miller, W.R.** (2009). The use of HMDS (hexamethyldisilazane) to replace Critical Point Drying (CPD) in the preparation of tardigrade for SEM (Scanning Electron Microscope) imaging. *Trans. Kans. Acad. Sci.* **112**:198–200.
- Sochacki, K.A., and Taraska, J.W.** (2017). Correlative fluorescence super-resolution localization microscopy and platinum replica EM on unroofed cells. *Methods Mol. Biol.* **1663**:219–230. https://doi.org/10.1007/978-1-4939-7265-4_18.
- Sofroniew, N., Lambert, T., Evans, K., Nunez-Iglesias, J., Bokota, G., Bussonnier, M., Peña-Castellanos, G., Winston, P., Yamauchi, K., and Pop, D.D.** (2022). napari/napari: 0.4.14. <https://doi.org/10.5281/zenodo.5975474>.
- Stringer, C., Wang, T., Michaelos, M., and Pachitariu, M.** (2021). Cellpose: a generalist algorithm for cellular segmentation. *Nat. Methods* **18**:100–106. <https://doi.org/10.1038/s41592-020-01018-x>.
- Traas, J.A.** (1984). Visualization of the membrane bound cytoskeleton and coated pits of plant cells by means of dry cleaving. *Protoplasma* **119**:212–218. <https://doi.org/10.1007/BF01288875>.
- Ungewickell, E., and Branton, D.** (1981). Assembly units of clathrin coats. *Nature* **289**:420–422. <https://doi.org/10.1038/289420a0>.
- van der Valk, P., Rennie, P.J., Connolly, J.A., and Fowke, L.C.** (1980). Distribution of cortical microtubules in tobacco protoplasts. An immunofluorescence microscopic and ultrastructural study. *Protoplasma* **105**:27–43. <https://doi.org/10.1007/BF01279847>.
- Wang, J., Yperman, K., Grones, P., Jiang, Q., Dragwidge, J., Mylle, E., Mor, E., Nolf, J., Eeckhout, D., De Jaeger, G., et al.** (2021). Conditional destabilization of the TPLATE complex impairs endocytic internalization. *Proc. Natl. Acad. Sci. USA* **118**, 2023456118. <https://doi.org/10.1073/pnas.2023456118>.